X-ray photoemission study of Sr_2FeMoO_6 and $SrMoO_4$ films epitaxially grown on MgO(001): Near-surface chemical-state composition analysis

H. Jalili,[1] N. F. Heinig,[2] and K. T. Leung[1,2]
[1]*Department of Physics, University of Waterloo, Waterloo, Ontario, Canada N2L 3G1*
[2]*WATLab and Department of Chemistry, University of Waterloo, Waterloo, Ontario, Canada N2L 3G1*
(Received 16 December 2008; revised manuscript received 16 March 2009; published 20 May 2009)

Thin films of the double perovskite ferromagnet Sr_2FeMoO_6 have been grown on MgO(001) substrates by pulsed laser deposition at temperatures as low as 600 °C. High-resolution X-ray diffraction studies revealed that the deposited films are single-phase Sr_2FeMoO_6 epitaxially grown on the MgO substrate. The film grown at 800 °C was post-annealed in oxygen producing epitaxial films of $SrMoO_4$ on top of the Sr_2FeMoO_6 film. The corresponding magnetization data showed that the post-annealing treatment lowered the saturation magnetic moment from $3.4\mu_B$ per formula unit (or /f.u.) for the as-grown Sr_2FeMoO_6 film to $1.4\mu_B$/f.u. after annealing. X-ray photoemission measurements as a function of sputtering time further revealed the presence of $SrMoO_4$ on both the as-grown and annealed films and their corresponding depth profiles indicated a thicker $SrMoO_4$ overlayer on the annealed film. The intensity ratios of the $3d$ features of Mo^{4+}, Mo^{5+}, and Mo^{6+} for Sr_2FeMoO_6 remained unchanged with sputtering depth (after 160 s of sputtering) strongly suggesting that the observed secondary phase ($SrMoO_4$) was formed predominantly on the surface and not in the subgrain boundaries of the as-grown Sr_2FeMoO_6 film. The presence of the secondary phase on the surface of the as-grown Sr_2FeMoO_6 film therefore plays a major role in contributing to the observed lower value for the saturation magnetic moment than the theoretical value.

DOI: 10.1103/PhysRevB.79.174427 PACS number(s): 75.70.Ak, 79.60.Dp, 81.15.Fg

I. INTRODUCTION

The double perovskite Sr_2FeMoO_6 has long been known as a conducting ferromagnet (or ferrimagnet) with a relatively high Curie temperature (T_C) of 410–450 K.[1] In 1998, Kobayashi *et al.*[2] showed that half-metallic Sr_2FeMoO_6 has a low-field magnetoresistance (LFMR) response at room temperature, which stimulated a great deal of research activity on this prospective material for spintronics applications. The double perovskite crystal structure consists of two interpenetrating face-centered-cubic sublattices. An ordered arrangement of Fe^{3+} ($3d^5$ and $S=\frac{5}{2}$) magnetic moments antiferromagnetically coupled to the Mo^{5+} ($4d^1$ and $S=\frac{1}{2}$) moments gives a total saturation magnetic moment of $4\mu_B$ at low temperature. However, it has thus far been difficult to prepare Sr_2FeMoO_6 samples with this high magnetic moment with most of the experimental moments ($2.2-3.9\mu_B$ per formula unit or /f.u.) reported to date being less than this expected value.[3–6] The origin of LFMR and low saturation magnetic moment were commonly attributed to two main types of defects, antisite defects and grain boundaries, and they have attracted much attention from many groups in the past decade.[3–9]

Defined as the misplacement of Fe ions with Mo ions, antisite defects have been shown to affect the transport and magnetic properties of Sr_2FeMoO_6.[8,10–12] Garcia-Hernandez *et al.*[8] reported that disorder at the Fe and Mo sites was responsible for the linear dependence of the saturation magnetization on the LFMR in bulk Sr_2FeMoO_6. By annealing the Sr_2FeMoO_6 samples in H_2/Ar at different temperatures, Navarro *et al.*[10] produced bulk samples with different concentrations of antisite defects. They suggested that antisite defects could promote magnetic frustration, lower the magnetic moments, and could also be responsible for the high-field magnetoresistance (MR). Saha-Dasgupta *et al.*[11] used *ab initio* band-structure calculations to show that the presence of antisite defects destroyed the half-metallic nature of Sr_2FeMoO_6 and reduced the magnetic moments at the Fe sites. Furthermore, Monte Carlo calculations by Ogale *et al.*[12] demonstrated that both the saturation magnetic moment and T_C of Sr_2FeMoO_6 strongly depended on the antisite defect density and that the oxygen content could play an important role in the magnitude of the magnetic moment, especially in samples with more disorder.

The other common types of defects that could account for LFMR in Sr_2FeMoO_6 are secondary phases and antiphase grain boundaries.[2,4,5,7,13–16] Sarma *et al.*[14] measured high-field and low-field MR for ordered and disordered bulk Sr_2FeMoO_6 samples and showed that the disordered sample was not half metallic and only the ordered sample exhibited a sharp LFMR peak. They concluded that the observed LFMR was dominated by intergrain spin-dependent scattering of highly polarized charge carriers in this half metal. For Sr_2FeMoO_6 films grown on $SrTiO_3$(100) bicrystals, Yin *et al.*[5] also attributed the LFMR to spin-dependent scattering across grain boundaries and not to an intragranular effect. In contrast, Huang *et al.*[4] compared the transport and magnetic properties of a series of bulk Sr_2FeMoO_6 samples with different grain sizes and disorder and with homocomposite samples (consisting of mixtures of perfectly ordered Sr_2FeMoO_6 as the main component and less-ordered Sr_2FeMoO_6 as the second or third component). Those samples with larger grain size and lower disorder were found to have higher saturation magnetic moments and MR. The homocomposite samples with a large amount of grain boundaries also showed large LFMR. They therefore concluded that both intergranular and intragranular effects were responsible for LFMR. Niebieskikwiat *et al.*[7] showed that for poly-

crystalline bulk $Sr_2FeMoO_{6+\delta}$ samples, the magnetization and lattice parameters were the same but the MR was enhanced for $\delta=0.04$. This latter result led them to propose that extra oxygen near the surface of the grain boundary was responsible for the enhancement. Zhong *et al.*[15] used a wet-chemistry method to produce Sr_2FeMoO_6 "bulrushlike" nanostructures. They showed that the MR could be improved by controlling the grain size and the concentration of $SrMoO_4$ at the grain boundary. The presence of $SrMoO_4$ at the grain boundary was also suggested by MacManus-Driscoll *et al.*[16]

Due to the sensitivity of the magnetic and transport properties to crystal defects such as the aforementioned antisite defects and grain boundaries, the methodologies and conditions of sample preparation are very important for controlling the physical properties of the Sr_2FeMoO_6 films. Although a number of methods including solid-state reaction, wet chemistry, and magnetron sputtering[10,15,17,18] have been used successfully to grow Sr_2FeMoO_6 films, pulsed laser deposition (PLD) is the most commonly used method. The most popular substrate for growing Sr_2FeMoO_6 films is $SrTiO_3(100)$ due to the close lattice matching between the two materials.[19] The possible presence of oxygen deficiency[20] and low-level magnetic impurities in the $SrTiO_3$ substrate could, however, lead to unusual electrical behavior potentially causing difficulties in interpreting the data. Other substrates, including MgO(001) (Refs. 18 and 21) and $LaAlO_3(100)$,[5] have also been used to obtain epitaxially grown Sr_2FeMoO_6 films. For Sr_2FeMoO_6 films epitaxially grown on $SrTiO_3(100)$ and $LaAlO_3(100)$, Yin *et al.*[5] found their magnetic and transport properties to be independent of the substrates. However, Asano *et al.*[18] and Borges *et al.*[21] showed that the magnetic and transport properties of epitaxial Sr_2FeMoO_6 films on $SrTiO_3$ and MgO were different with smaller magnetic moments found on MgO [$1.0\mu_B$/f.u. at 300 K (Ref. 18) and $2.3\mu_B$/f.u. at 20 K (Ref. 21)] than on $SrTiO_3$ [$1.3\mu_B$/f.u. at 300 K (Ref. 18) and $3.5\mu_B$/f.u. at 20 K (Ref. 21)].

In addition to obtaining a good quality film, another challenge in the fabrication of spintronic devices is to grow defect-free multilayer films with high-quality interfaces to prevent scattering during the extraction of polarized spins. In the case of Sr_2FeMoO_6, the presence of grain boundaries has already been found to affect the LFMR.[4,5,7] The surface electronic structure of polycrystalline Sr_2FeMoO_6 (Refs. 22 and 23) and Sr_2FeMoO_6 thin films epitaxially grown on $SrTiO_3$ (Refs. 24 and 25) have been reported. However, the formation of a secondary phase on the surface of these samples could contribute to the core-shell photoemission spectra, particularly in the Mo 3*d* region, and therefore affect the electronic structure of the perceived interface. Systematic study of the electronic structure of the near-surface region by using depth-profiling X-ray photoelectron spectroscopy (XPS) analysis can provide further insight into the chemical-state composition of the film, which can then be used to improve the interface quality in multilayer film devices.

In the present work, we demonstrate that Sr_2FeMoO_6 films can be deposited by PLD on MgO(001) from 400 to 800 °C, and epitaxially grown films can be obtained at a temperature as low as 600 °C. MgO is chosen as the substrate because MgO has a reasonably good lattice match to Sr_2FeMoO_6 (with the lattice parameters within 6.2%, JCPDS 4–0829 and 70–4092). Because MgO is nonmagnetic, it will not introduce any magnetic signature. MgO can therefore be used as an inert support for constructing spin-based devices. The saturation magnetic moment is found to be almost the same ($3.4\mu_B$/f.u.) for Sr_2FeMoO_6 samples grown at 600 and 800 °C with the coercivity field of the former higher than the latter. The high quality of the Sr_2FeMoO_6 films grown at 800 °C is indicated not only by the low coercivity field and high saturation magnetic moment but also by the narrow width (0.3°) of the rocking curve of the (004) plane. In addition to the growth temperature, post-annealing in oxygen could also affect the near-surface quality of the Sr_2FeMoO_6 samples. We provide a detailed study of the electronic structure and chemical-state composition of the Sr_2FeMoO_6 film as grown on MgO(001) at 800 °C and upon annealing in oxygen by depth-profiling XPS. The XPS analyses for the as-grown and post-annealed samples both show the existence of $SrMoO_4$ as a secondary phase predominantly on the film surface and not in the subgrain boundaries in the bulk.

II. EXPERIMENTAL DETAILS

A NanoPLD system (PVD Products) with a base pressure of 5×10^{-7} Torr was used for the film growth experiments. The system was equipped with a KrF excimer laser (248 nm) with a maximum laser fluence of 600 mJ/pulse. An 1-inch-diameter Sr_2FeMoO_6 target (99.95% purity) was obtained commercially (MTI Corp.). A 5×10 mm^2 MgO(001) epi-polished substrate was mounted face down above the target with a target-to-substrate distance of 42 mm. The substrate was heated by infrared lamps irradiating the back side and the substrate temperature was monitored by a thermocouple and an optical pyrometer. With the substrate held at a preselected temperature between 400 and 800 °C, deposition was performed in vacuum for 30 min. A laser fluence of 400 mJ/pulse (corresponding to an energy density of 3–5 mJ/cm^2 delivered to the target) was used and the repetition rate was set to 10 Hz. For the post-annealing experiment, the sample was held at 800 °C in 10 mTorr of O_2 gas at a flow rate of 20 sccm for 40 min followed by 2 h of annealing at the same temperature in vacuum.

The morphology and stoichiometry of the as-grown and post-annealed films were characterized by using scanning electron microscopy (SEM, LEO FESEM-1530) and energy-dispersive X-ray spectrometry, respectively. To obtain the crystal structures of the as-grown films, high-resolution X-ray diffraction (XRD) data were collected with ω-2θ scans by using a PANalytical X'Pert Pro MRD X-ray diffractometer equipped with a two-bounce hybrid monochromator and a Cu K_α source for the incident-beam optics and a triple-axis section as the diffracted beam optics. To determine the film thickness, an X-ray reflectivity measurement was made with an X-ray mirror as the incident-beam optics and a parallel-plate collimator as the reflected beam optics. Magnetization data of the as-grown films were obtained by using a superconducting quantum interference device (SQUID) magnetometer (Quantum Design) capable of operating up to

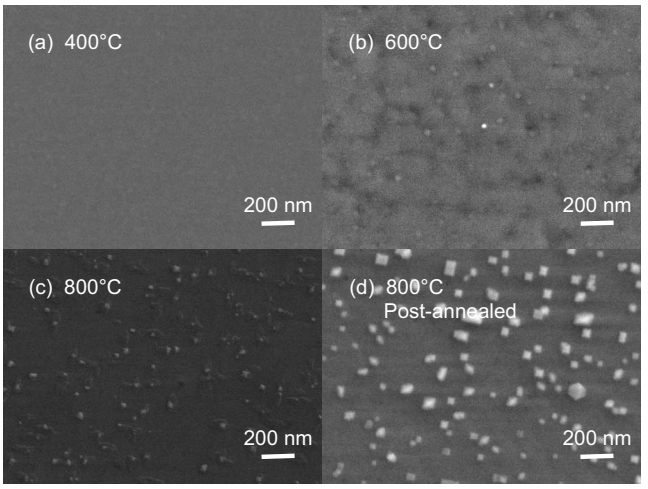

FIG. 1. SEM images of Sr_2FeMoO_6 PLD grown on MgO(001) in vacuum at (a) 400 °C, (b) 600 °C, (c) 800 °C, and (d) of sample (c) after post-annealing in O_2.

a 7 T magnetic field. The chemical-state composition of the films were studied by using a Thermo-VG Scientific ESCALab 250 X-ray photoelectron spectrometer, equipped with a monochromatic Al K_α X-ray source (1486.6 eV) at a typical energy resolution of 0.4–0.5 eV full width at half maximum (FWHM). For the depth-profiling experiments, argon sputtering was performed over a rastered area of 3×3 mm^2 of the sample at an ion-beam energy of 3 keV. Based on our earlier work on Fe/Fe oxide core-shell nanomaterials, we estimate that the sputtering rate to be ~0.9 nm/min.[26] The collected XPS data were fitted, where appropriate, with a combination of Gaussian-Lorentzian line shapes, after correction for the Shirley background, by using the CASA XPS software.

III. RESULTS AND DISCUSSION

A series of Sr_2FeMoO_6 film samples were grown in vacuum at several temperatures of 400, 500, 600, 700, and 800 °C and the resulting as-grown films all appeared as black. The SEM images for the films grown at 400, 600, and 800 °C shown in Fig. 1 reveal generally smooth surfaces with root-mean-square roughness of 0.6, 7.1, and 8 nm (over 12 μm^2), respectively, as measured by atomic force microscopy. Randomly distributed nanoparticles (<20 nm in size) are also found on top of the latter two films. Consistent with the XPS data, they may be attributed to oxides of Fe and Mo segregating on the surface during the deposition. The film grown at 800 °C has also been further annealed in O_2 using the procedure discussed earlier. Unlike the other as-grown films the post-annealed film appeared yellow-brown in color and was nonconducting. The corresponding SEM image [Fig. 1(d)] also shows a smooth surface with a greater number of larger nanoparticles (20–100 nm in size) mostly with a cubic shape. The presence of these cubic nanoparticles has also been reported by Besse *et al.*[27] who attributed them to iron oxide based on their XRD measurement. We also deposited a Sr_2FeMoO_6 film at 800 °C in an argon atmosphere of

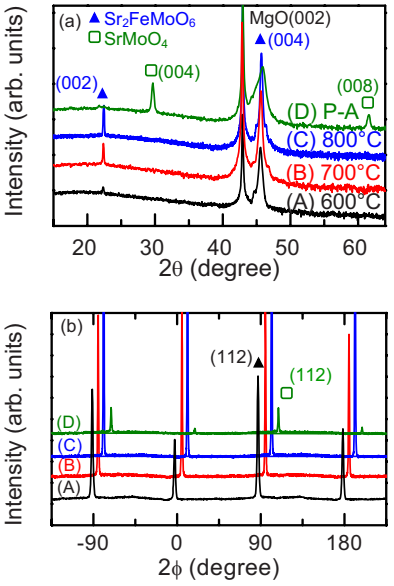

FIG. 2. (Color online) (a) ω-2θ scans of Sr_2FeMoO_6 films PLD grown on MgO(001) in vacuum at (A) 600 °C, (B) 700 °C, and (C) 800 °C. The top curve (D) corresponds to sample (C) post-annealed in 10 mTorr of O_2. All data are plotted with a logarithmic y axis with the curves offset for clarity. (b) Corresponding ϕ scans of (A, B, and C) the Sr_2FeMoO_6(112) plane (2θ=32.01°, ω=16.00°, and ψ=45.08°) and (D) $SrMoO_4$(112) plane (2θ=27.67°, ω=13.84°, and ψ=57.60°).

10 mTorr (not shown) and the resulting film did not show any discernible difference from the film shown in Fig. 1(c), which was grown in vacuum.

Figure 2(a) shows the ω-2θ XRD scans for films grown at 600, 700, and 800 °C before and after annealing in O_2. In addition to the strong (002) peak of the MgO substrate at 42.9° (JCPDS 4–0829), the strong peak at 45.7° and the weaker peak at 22.4° can be attributed, respectively, to the (004) and (002) planes of Sr_2FeMoO_6 (JCPDS 70–4092). Evidently, a single-phase epitaxial Sr_2FeMoO_6 film has already been formed at a deposition temperature as low as 600 °C. Rocking curve analysis of the (004) plane of the as-grown films (not shown) indicates that the peak width narrowed from 1.1° FWHM for the film grown at 600 °C to 0.3° FWHM for the film grown at 800 °C, consistent with improved crystal quality for films grown at a higher temperature. Before post-annealing in O_2, the as-grown film at 800 °C consists of Sr_2FeMoO_6 oriented with the (001) direction parallel to the MgO(001) plane. After post-annealing in O_2, the amount of Sr_2FeMoO_6 is reduced and two new peaks at 29.7° and 61.5°, attributed to the (004) and (008) planes of $SrMoO_4$ (JCPDS 70–2537), are observed [Fig. 2(a), top curve]. This indicates the formation of a significant amount of an oriented $SrMoO_4$ phase with its (001) plane parallel to the MgO(001) plane [as well as to the (001) plane of Sr_2FeMoO_6], upon post-annealing in O_2. For the samples grown at a temperature lower than 600 °C [e.g., Fig. 1(a)], no features other than the substrate peaks are observed, despite the presence of discernible films on the substrates. The lack of any observable Sr_2FeMoO_6 peaks may be due to the formation of an amorphous or randomly oriented polycrys-

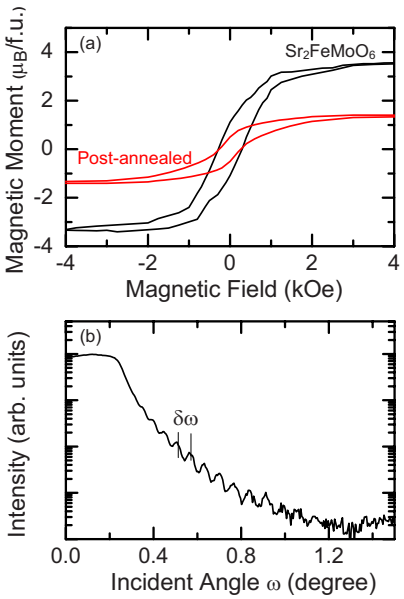

FIG. 3. (Color online) (a) Magnetization as a function of applied magnetic field for a Sr_2FeMoO_6 film PLD grown on MgO(001) in vacuum at 800 °C and upon post-annealing in O_2. (b) X-ray reflectivity measurement of the as-grown Sr_2FeMoO_6 film at 800 °C as a function of incident angle.

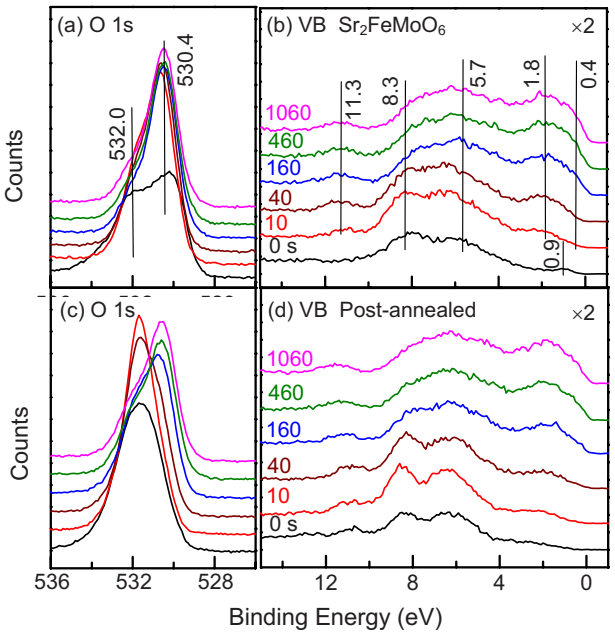

FIG. 4. (Color online) XPS spectra of (a,c) O 1*s* and (b,d) valence band (VB) regions as a function of sputtering time for the PLD-grown Sr_2FeMoO_6 film on MgO(001) at 800 °C (a,b) before and (c,d) after post-annealing in O_2.

talline Sr_2FeMoO_6 film on the MgO(001) substrate.

Figure 2(b) shows the ϕ scans for the Sr_2FeMoO_6(112) plane, corresponding to the diffraction peak at $2\theta=32.01°$, $\omega=16.00°$, and $\psi=45.08°$, for the films grown at 600, 700, and 800 °C. The presence of four equally spaced diffraction peaks indicates that the Sr_2FeMoO_6 films form epitaxial single crystals on the MgO and not just *c* axis aligned polycrystalline films. A similar ϕ scan for the $SrMoO_4$(112) plane, corresponding to the diffraction peak at $2\theta=27.67°$, $\omega=13.84°$, and $\psi=57.60°$, for the 800 °C sample post-annealed in O_2 is also shown. As with Sr_2FeMoO_6, the four-fold symmetry of the (112) plane for $SrMoO_4$ indicates that this material is also epitaxially aligned with the MgO substrate.

The magnetization curves for the as-grown film at 800 °C before and after annealing in O_2 have been measured at 5 K for a magnetic field up to 5 kOe by using a SQUID magnetometer and are shown in Fig. 3(a). The magnetic field was applied parallel to the film surface. The diamagnetic signal due to the MgO(001) substrate has been removed from the data. In order to calculate the saturation magnetic moment, the film thickness is required and may be deduced from a measurement of the X-ray reflectivity for the as-grown film shown in Fig. 3(b). The thickness of the film (t) is related to the separation between interference fringes ($\delta\omega$, in radian) by the formula: $t=\frac{\lambda}{2\delta\omega}$ where λ is the wavelength of the X ray (1.54 Å for Cu K_α). The presence of well-defined fringes also indicates that the film thickness is almost constant over the entire film and the film surface is smooth. Using the film thickness obtained from the reflectivity measurements (98 nm) and the dimensions of the sample area measured by a micrometer, the maximum-saturation magnetic moments are found to be $3.4\pm0.1\mu_B$/f.u. for the as-grown film and $1.4\pm0.1\mu_B$/f.u. upon post-annealing. The saturation magnetic moment of the Sr_2FeMoO_6 film as grown on MgO(001) is therefore considerably larger than the values reported earlier [$1.0\mu_B$/f.u. at 300 K (Ref. 18) and $2.3\mu_B$/f.u. at 20 K (Ref. 21)] which indicates the superior quality of the as-grown film. The formation of $SrMoO_4$ upon post-annealing of the as-grown film reduces the saturation magnetic moment, which could be a major contributing factor to the lower saturation magnetic moment found in the earlier work. However, the coercive fields (0.56 kOe) for both the as-grown and post-annealed films are found to be the same [Fig. 3(a)], supporting the result from the ϕ scans in Fig. 2(b) that post-annealing in O_2 has no effect on grain formation. The coercive field for the film grown at 600 °C was also measured (not shown) and the larger value (1.2 kOe) is consistent with the rocking curves with larger FWHMs found in samples grown at a lower temperature.

Figure 4 compares the XPS spectra of the valence band (VB) and O 1*s* regions as a function of sputtering time for the as-grown Sr_2FeMoO_6 film before and after annealing in O_2. For the as-grown Sr_2FeMoO_6 film, three well-defined features at 0.9, 5.7, and 8.3 eV can be observed [Fig. 4(b)]. Sputtering the film for 10 s appears to remove the feature at 0.9 eV and strengthen the features at 5.7 and 8.3 eV and to expose two new features at 1.8 and 11.3 eV. Further sputtering for 40 s sharpens all four features and a small shoulder is seen to emerge at 0.4 eV. Continued sputtering for extended periods (over 160 s) substantially reduces the feature at 8.3 eV, while all other features at 0.4, 1.8, 5.7, and 11.3 eV remain essentially unchanged. The depth profiles of these valence-band features suggest that the "overlayer" region, with a discernibly different composition from the bulk region, can be removed after ~40 s of sputtering. The ob-

served features at 0.4, 1.8, 5.7, 8.3, and 11.3 eV are found to be in good accord with the photoemission measurement made for polycrystalline Sr_2FeMoO_6 by Ray *et al.*[28] Their *ab initio* calculations further showed that their observed features near 0.4, 1.8, 5.7, and 8.3 eV originate from the Mo 4*d*, Fe 3*d*, O 2*p*, and Mo 4*d* bands, respectively. Similar assignments have also been made by Kuepper *et al.*[22] in their combined study involving XPS and a local-density-approximation band-structure calculation of polycrystalline Sr_2FeMoO_6 and by Saitoh *et al.*[29] and Navarro *et al.*[30] For the feature at 11.3 eV, Saitoh *et al.*[29] proposed that a similar feature near 12.2 eV to be most probably due to oxygen states of suboxides on the surface while Navarro *et al.*[30] suggested the broad feature in 9–12 eV to be related to Fe-O hybridized states.

For the Sr_2FeMoO_6 film after the post-annealing treatment, the evolution of the observed features with sputtering [Fig. 4(d)] appears to be similar to that of the as-grown film [Fig. 4(b)]. The notably stronger relative intensity of the feature at 8.3 eV for the post-annealed film [Fig. 4(d)] than that of the as-grown film after 40 s of sputtering [Fig. 4(b)] suggests a thicker overlayer region for the former.

The difference in the overlayer region of the as-grown Sr_2FeMoO_6 film before and after annealing can be better illustrated in their respective O 1*s* XPS spectra. In particular, two peaks at 530.4 and 532.0 eV with nearly equal intensities can be observed for the as-grown film [Fig. 4(a)]. Just 10 s of sputtering appears to reduce the feature at 532.0 eV and to substantially enhance the feature at 530.4 eV. The spectrum becomes essentially unchanged after further sputtering for 40 s. In contrast, the O 1*s* spectrum of the annealed film exhibits a singular intense feature at 532.0 eV [Fig. 4(c)]. Only after sputtering for 160 s has the feature at 532.0 eV been reduced sufficiently to expose the feature at 530.4 eV, the intensity of which remains unchanged upon further sputtering. The observed evolution of these O 1*s* features with respect to sputtering time (depth) is consistent with a thicker overlayer found for the annealed film than that for the as-deposited film, as inferred earlier from the valence-band spectra [Figs. 4(b) and 4(d)]. Based on the XRD spectra of the annealed film (Fig. 2, curve D), the overlayer can be attributed to $SrMoO_4$. Given the detection limit of XRD is about 1% (for the bulk), the lack of $SrMoO_4$ XRD features in the as-grown film (Fig. 2) is consistent with the thin $SrMoO_4$ overlayer as reflected in the depth-profiling XPS spectra (with a detection limit of 0.5% for the surface). It should be noted that the notable increase in the overall spectral intensity for the 10 s spectra (for both as-grown and annealed films) relative to the original spectra (i.e., before sputtering) is due to the removal of the surface carbonaceous layer commonly found on materials exposed to air.

Figure 5 shows the corresponding XPS spectra of Sr 3*d* and Fe 2*p* regions for the as-grown Sr_2FeMoO_6 film before and after annealing. Evidently, both samples exhibit a doublet of Sr $3d_{5/2}$ ($3d_{3/2}$) at 133.7 eV (135.5 eV) with a spin-orbit splitting of 1.8 eV and an expected intensity ratio of 3:2 [Figs. 5(b) and 5(d)]. The binding-energy positions of these Sr 3*d* features are in good accord with the literature values for Sr^{2+} in a perovskite structure.[31,32] Sputtering did not appear to change the overall intensity or the profile of the doublet, which indicates that the $SrMoO_4$ overlayer and the Sr_2FeMoO_6 film have similar local chemical environments for the Sr atoms. Sr is coordinated to four Mo atoms in the tetragonal hole in $SrMoO_4$ (Ref. 33) and to four Mo and four Fe atoms in the tetragonal hole in the Sr_2FeMoO_6 lattice. However, given the fact that a Mo atom is larger and has more electrons than a Fe atom, the local Sr chemical environment in Sr_2FeMoO_6 is expected to be dominated by the larger Mo atoms. The prominence of the Mo electron densities in Sr_2FeMoO_6 apparently leads to Sr 3*d* binding-energy shifts that are too small to be distinguishable from those in the $SrMoO_4$ overlayer and therefore not detectable by our present XPS system.

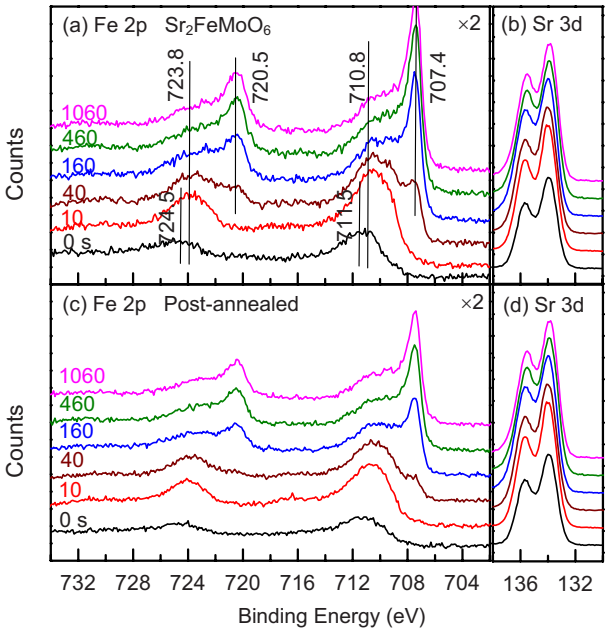

FIG. 5. (Color online) XPS spectra of (a,c) Fe 2*p* and (b,d) Sr 3*d* regions as a function of sputtering time for the PLD-grown Sr_2FeMoO_6 film on MgO(001) at 800 °C (a,b) before and (c,d) after post-annealing in O_2.

The depth-profiling Fe 2*p* XPS spectra for the as-grown Sr_2FeMoO_6 film [Fig. 5(a)] are also found to be essentially the same as those of the film after annealing [Fig. 5(c)]. In particular, the as-deposited film exhibits a doublet of Fe $2p_{3/2}$ ($2p_{1/2}$) at 710.8 eV (723.8 eV), the intensity of which increased upon sputtering above 10 s. The binding energies of this doublet are between the reported values for Fe^{3+} and Fe^{2+} oxidation states.[34] This result therefore suggests an oxidation state of $Fe^{(3-\delta)+}$ for Sr_2FeMoO_6 in good accord with that found for Sr_2FeMoO_6 by X-ray absorption spectroscopy.[23] For the as-grown film and that after 10 s of sputtering, an additional doublet at 711.5 eV (724.5 eV), corresponding to the Fe^{3+} oxidation state of Fe_2O_3,[26,34] is needed to account for the extra spectral intensity at the higher binding-energy side. The existence of this doublet only in the as-deposited film and that after 10 s of sputtering strongly suggests that the nanoparticles on the surface of the as-grown film, as shown in the SEM image in Fig. 1(c), are primarily Fe_2O_3. After sputtering for 40 s, a sharp doublet at 707.4 eV (720.5 eV) is found and becomes the prominent

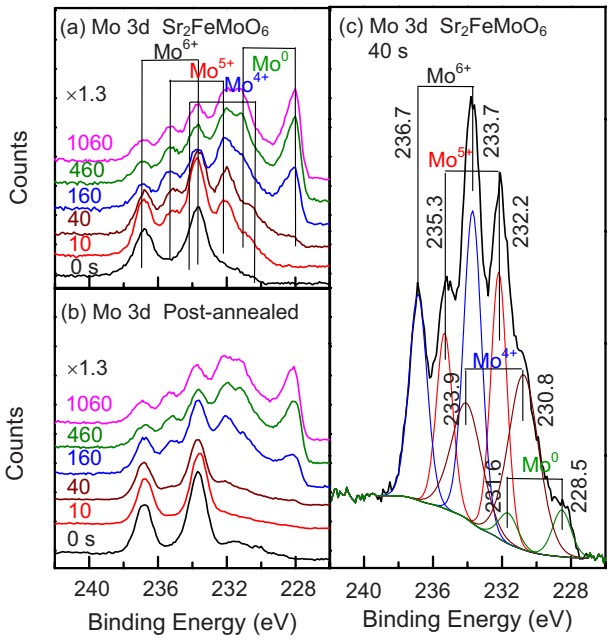

FIG. 6. (Color online) XPS spectra of Mo 3*d* region as a function of sputtering time for the PLD-grown Sr_2FeMoO_6 film on MgO(001) at 800 °C (a) before and (b) after post-annealing in O_2. (c) Peak fitting of the spectrum for the as-grown Sr_2FeMoO_6 film after 40 s of argon sputtering.

feature upon further sputtering above 160 s. This lowest-binding-energy feature can be attributed to metallic Fe (Fe^0) which is produced by reduction in the higher Fe oxidation states due to Ar ion sputtering.[26,35] It should be noted that the lack of a metallic Fe peak for the as-grown film [Fig. 5(a)] confirms the high film quality of the present PLD-grown Sr_2FeMoO_6 film and the absence of any significant amount of Fe phase in the film, in contrast to the earlier work that reported an additional metallic Fe peak for their as-deposited film.[24] Furthermore, the nearly identical intensity evolution with respect to sputtering time found for both as-grown [Fig. 5(a)] and post-annealed films [Fig. 5(c)] suggests that the cubic nanoparticles seen in the post-annealed film in Fig. 1(d) also consist of Fe_2O_3, which has the Fe^{3+} oxidation state close to that found for Sr_2FeMoO_6.[23] The decrease in the saturation magnetic moment in the post-annealed film [Fig. 3(a)] is consistent with the nanoparticles mainly consisting of antiferromagnetic α-Fe_2O_3.

Figure 6 compares the XPS spectra of the Mo 3*d* region as a function of sputtering time for the as-grown Sr_2FeMoO_6 film before and after annealing, both of which depict evolution of rather complex sets of peaks. In Fig. 6(c), we select the spectrum for the as-grown film after 40 s of sputtering as the spectrum representative of the interface region in order to illustrate the fitting of the complex spectral envelope into four sets of Mo $3d_{5/2}$ ($3d_{3/2}$) doublets. A spin-orbit splitting of 3.1 eV (Ref. 36) and a $3d_{5/2}$:$3d_{3/2}$ intensity ratio of 3:2 have been used for the fitting after appropriate correction of the background with a single Shirley (Gaussian-step) function. Using the literature values for different Mo oxides,[23,34,36] we assign the observed Mo $3d_{5/2}$ ($3d_{3/2}$) features at 228.5 eV (231.6 eV), 230.8 eV (233.9 eV), 232.2 eV

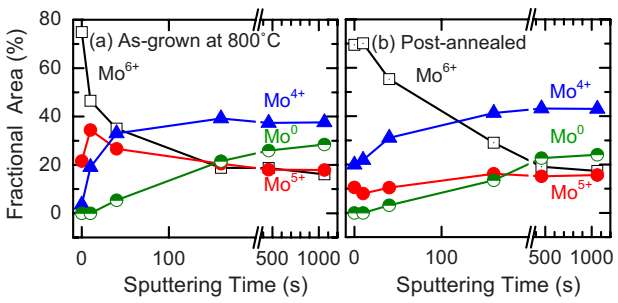

FIG. 7. (Color online) Fractional area of Mo^{n+} (with respect to the area of the overall Mo 3*d* spectrum) as a function of sputtering time for the PLD-grown Sr_2FeMoO_6 film on MgO(001) at 800 °C (a) before and (b) after post-annealing in O_2.

(235.3 eV), and 233.7 eV (236.7 eV) to Mo^0 (i.e., metallic Mo), Mo^{4+}, Mo^{5+}, and Mo^{6+} states, respectively. An excellent fit has been obtained when the peak widths for the Mo^0, Mo^{4+}, Mo^{5+}, and Mo^{6+} features were set to 1.0 ± 0.2 eV, 2.4 ± 0.2 eV, 1.2 ± 0.2 eV, and 1.3 ± 0.2 eV FWHM, respectively. Although the peak widths are inherently related to the natural lifetimes of the states, the larger widths found for the Mo^{4+} features could be due to the presence of close-lying many-body states or defect states as hypothesized by Kuepper *et al.*[22] It should be noted that the Mo 3*d* spectrum shown in Fig. 6(c) is in excellent accord with the experimental[14,22] and calculated spectra[14] of polycrystalline Sr_2FeMoO_6 reported in the literature.

The depth profiles of the fitted areas for the Mo^0, Mo^{4+}, Mo^{5+}, and Mo^{6+} $3d_{5/2}$ features with respect to the total area of the spectrum are shown for both as-grown and post-annealed films in Fig. 7(a). Before sputtering, the as-grown Sr_2FeMoO_6 film exhibits primarily the strong Mo^{6+} features [Fig. 6(a)] with the other Mo features appearing only as a weak shoulder at the lower binding-energy side. Upon sputtering for 10 to 160 s, the intensities of the Mo^{6+} features are reduced while those for the Mo^{5+} features are enhanced dramatically. In the meantime, the removal of the prominent Mo^{6+} features has exposed the underlying Mo^{4+} features. The intensities of Mo^{5+} features appear to undergo a more gradual reduction upon sputtering for 10 s to 160 s than those for Mo^{6+} features. Further sputtering above 160 s appears not to affect the relative intensities of the Mo^{4+}, Mo^{5+}, and Mo^{6+} [Fig. 7(a)] and the spectral envelope remains relatively stable [Fig. 6(a)]. Like the Fe 2*p* features (Fig. 5) the emergence of the metallic Mo^0 features at 228.5 eV (231.6 eV) after 40 s of sputtering (Fig. 6) can be attributed to reduction of the higher oxidation states by Ar ion sputtering. The metallic Mo features could also introduce additional uncertainty to the relative intensities of the other Mo states for the spectra with sputtering for longer than 40 s. The intensities of the metallic Mo features also become nearly constant after sputtering longer than 460 s [Fig. 7(a)].

For the Sr_2FeMoO_6 film post-annealed in O_2, the corresponding spectral evolution of the Mo $3d_{5/2}$ ($3d_{3/2}$) features as a function of sputtering time, shown in Figs. 6(b) and 7(b), is found to be similar to that of the as-grown film [Figs. 6(a) and 7(a)]. In particular, the relative intensities of the Mo^{4+}, Mo^{5+}, and Mo^{6+} states appear to reach nearly the same

stable values after 460 s of sputtering for the films before and after the post-annealing (Fig. 7). Interestingly, a similar observation has been made for polycrystalline Sr_2FeMoO_6 grown on a Si substrate.[37] These results suggest that the $SrMoO_4$ growth occurs largely on the surface and not in the subgrain boundaries of the bulk, which confirms our earlier hypothesis that the reduction in the saturation magnetic moment [Fig. 3(a)] is due to the formation of $SrMoO_4$ (and α-Fe_2O_3) on the surface and not in the bulk. A notable difference between the two depth profiles (Fig. 7) is that there appears to be a latent period (of ~10 s of sputtering) before the onset of the changes for the post-annealed film [Fig. 7(b)]. Consistent with the presence of $SrMoO_4$ in the XRD data of the post-annealed film [Fig. 2(a)], this indicates a thicker $SrMoO_4$ overlayer for the post-annealed film, which primarily gives rise to the Mo^{6+} features. The similarity of Mo 3*d* spectra for the as-grown film before and after the post-annealing without any sputtering [Figs. 6(a) and 6(b)] suggests that the formation of $SrMoO_4$ on the surface of the as-grown Sr_2FeMoO_6 film occurs readily upon exposure to air.

IV. CONCLUDING REMARKS

In summary, thin films of Sr_2FeMoO_6 have been grown on MgO(001) substrates at several temperatures (400, 500, 600, 700, and 800 °C) by pulsed laser deposition. High-resolution X-ray diffraction studies reveal epitaxial growth of a single-phase (double perovskite) Sr_2FeMoO_6 film on MgO(001) at a temperature as low as 600 °C with the best film quality obtained at 800 °C. The film grown at 800 °C was subsequently annealed in O_2 producing an additional epitaxial overlayer of $SrMoO_4$ on the Sr_2FeMoO_6 film. The magnetization data showed that the post-annealing treatment lowered the saturation magnetic moment from $3.4\mu_B$/f.u. to $1.4\mu_B$/f.u. with no discernible change in the observed coercive fields (0.56 kOe). This result indicates that post-annealing in O_2 has no notable effect on the grain formation in the bulk and suggests that the (thicker) $SrMoO_4$ overlayer and antiferromagnetic α-Fe_2O_3 nanoparticles are responsible for the observed reduction in the saturation magnetic moment. Furthermore, the lower optimal saturation magnetic moment ($3.4\mu_B$/f.u.) obtained for the as-grown Sr_2FeMoO_6 film than the expected value ($4.0\mu_B$/f.u.) could also be due to the presence of a thin $SrMoO_4$ overlayer that formed upon exposure to air. To study the film quality and chemical-state composition of the near-surface region, depth-profiling X-ray photoemission measurements of the valence-band, O 1*s*, Sr 3*d*, Fe 2*p*, and Mo 3*d* regions have been performed on the as-grown and post-annealed films. The similarity in the respective depth profiles supports the formation of $SrMoO_4$ overlayers on the surfaces of both the as-grown and post-annealed Sr_2FeMoO_6 films, the thickness of which was found to be greater in the post-annealed film. Furthermore, the intensity ratios of the 3*d* features of Mo^{4+}, Mo^{5+}, and Mo^{6+} for Sr_2FeMoO_6 remain unchanged with sputtering depth (after 160 s), supporting the model that the observed secondary phase ($SrMoO_4$) is formed predominantly on the surface and not in the subgrain boundaries of the as-grown Sr_2FeMoO_6 film.

[1] F. S. Galasso, *Structure, Properties, and Preparation of Perovskite-type Compounds* (Pergamon, London, 1969).
[2] K.-I. Kobayashi, T. Kimura, H. Sawada, K. Terakura, and Y. Tokura, Nature (London) **395**, 677 (1998).
[3] Y. Tomioka, T. Okuda, Y. Okimoto, R. Kumai, K.-I. Kobayashi, and Y. Tokura, Phys. Rev. B **61**, 422 (2000).
[4] Y.-H. Huang, H. Yamauchi, and M. Karppinen, Phys. Rev. B **74**, 174418 (2006).
[5] H. Q. Yin, J.-S. Zhou, J.-P. Zhou, R. Dass, J. T. McDevitt, and J. B. Goodenough, Appl. Phys. Lett. **75**, 2812 (1999).
[6] A. Di Trolio, R. Larciprete, A. M. Testa, D. Fiorani, P. Imperatori, S. Turchini, and N. Zema, J. Appl. Phys. **100**, 013907 (2006).
[7] D. Niebieskikwiat, A. Caneiro, R. D. Sanchez, and J. Fontcuberta, Phys. Rev. B **64**, 180406(R) (2001).
[8] M. Garcia-Hernandez, J. L. Martinez, M. J. Martinez-Lope, M. T. Casais, and J. A. Alonso, Phys. Rev. Lett. **86**, 2443 (2001).
[9] L. I. Balcells, J. Navarro, M. Bibes, A. Roig, B. Martinez, and J. Fontcuberta, Appl. Phys. Lett. **78**, 781 (2001).
[10] J. Navarro, L. I. Balcells, F. Sandiumenge, M. Bibes, A. Roig, B. Martinez, and J. Fontcuberta, J. Phys.: Condens. Matter **13**, 8481 (2001).
[11] T. Saha-Dasgupta and D. D. Sarma, Phys. Rev. B **64**, 064408 (2001).
[12] A. S. Ogale, S. B. Ogale, R. Ramesh, and T. Venkatesan, Appl. Phys. Lett. **75**, 537 (1999).
[13] Y. Sui, X. Zhang, X. Wang, J. Cheng, W. Su, and J. Tang, J. Appl. Phys. **102**, 023903 (2007).
[14] D. D. Sarma, E. V. Sampathkumaran, S. Ray, R. Nagarajan, S. Majumdar, A. Kumar, G. Nalini, and T. N. Guru Row, Solid State Commun. **114**, 465 (2000); D. D. Sarma, P. Mahadevan, T. Saha-Dasgupta, S. Ray, and A. Kumar, Phys. Rev. Lett. **85**, 2549 (2000).
[15] W. Zhong, W. Liu, C. T. Au, and Y. W. Du, Nanotechnology **17**, 250 (2006).
[16] J. L. MacManus-Driscoll, A. Sharma, Y. Bugoslavsky, W. Branford, L. F. Cohen, and M. Wei, Adv. Mater. **18**, 900 (2006).
[17] H. Suwaki, T. Yamaguchi, W. Sakamoto, T. Yogo, K. Kikuta, and S. Hirano, J. Magn. Magn. Mater. **295**, 230 (2005).
[18] H. Asano, M. Osugi, Y. Kohara, D. Higashida, and M. Matsui, Jpn. J. Appl. Phys., Part 1 **40**, 4883 (2001).
[19] T. Manako, M. Izumi, Y. Konishi, K.-I. Kobayashi, M. Kawasaki, and Y. Tokura, Appl. Phys. Lett. **74**, 2215 (1999).
[20] K. Szot, W. Speier, R. Carius, U. Zastrow, and W. Beyer, Phys. Rev. Lett. **88**, 075508 (2002).
[21] R. P. Borges, S. Lhostis, M. A. Bari, J. J. Versluijs, J. G. Lunney, J. M. D. Coey, M. Besse, and J.-P. Contour, Thin Solid Films **429**, 5 (2003).
[22] K. Kuepper, M. Kadiroglu, A. V. Postnikov, K. C. Prince, M. Matteucci, V. R. Galakhov, H. Hesse, G. Borstel, and M.

Neumann, J. Phys. Condens. Matter **17**, 4309 (2005); K. Kuepper, I. Balasz, H. Hesse, A. Winiarski, K. C. Prince, M. Matteucci, D. Wett, R. Szargan, E. Burzo, and M. Neumann, Phys. Status Solidi A **201**, 3252 (2004).

[23] D. Rubi, J. Navarro, J. Fontcuberta, M. Izquierdo, J. Avila, and M. C. Asensio, J. Phys. Chem. Solids **67**, 575 (2006) and references therein.

[24] J. Santiso, A. Figueras, and J. Fraxedas, Surf. Interface Anal. **33**, 676 (2002).

[25] T. Fix, A. Barla, C. Ulhaq-Bouillet, S. Colis, J. P. Kappler, and A. Dinia, Chem. Phys. Lett. **434**, 276 (2007).

[26] L. Y. Zhao, K. R. Eldridge, K. Sukhija, H. Jalili, N. F. Heinig, and K. T. Leung, Appl. Phys. Lett. **88**, 033111 (2006).

[27] M. Besse, F. Pailloux, A. Barthelemy, K. Bouzehouane, A. Fert, J. Olivier, O. Durand, F. Wyczisk, R. Bisaro, and J.-P. Contour, J. Cryst. Growth **241**, 448 (2002).

[28] S. Ray, P. Mahadevan, A. Kumar, D. D. Sarma, R. Cimino, M. Pedio, L. Ferrari, and A. Pesci, Phys. Rev. B **67**, 085109 (2003).

[29] T. Saitoh, M. Nakatake, A. Kakizaki, H. Nakajima, O. Morimoto, Sh. Xu, Y. Moritomo, N. Hamada, and Y. Aiura, Phys. Rev. B **66**, 035112 (2002).

[30] J. Navarro, J. Fontcuberta, M. Izquierdo, J. Avila, and M. C. Asensio, Phys. Rev. B **69**, 115101 (2004).

[31] R. Polini, A. Falsetti, E. Traversa, O. Schaf, and P. Knauth, J. Eur. Ceram. Soc. **27**, 4291 (2007).

[32] P. Wang, L. Yao, M. Wang, and W. Wu, J. Alloys Compd. **311**, 53 (2000).

[33] J. C. Sczancoski, L. S. Cavalcante, M. R. Joya, J. A. Varela, P. S. Pizani, and E. Longo, Chem. Eng. J. **140**, 632 (2008).

[34] J. F. Moulder, W. F. Stickle, P. E. Sobol, and K. D. Bomben, in *Handbook of X-ray Photoelectron Spectroscopy*, 2nd ed., edited by J. Chastain (Perkin-Elmer, Eden-Prairie, MN, 1992).

[35] T. Choudhury, S. O. Saied, J. L. Sullivan, and A. M. Abbot, J. Phys. D **22**, 1185 (1989).

[36] A. Katrib, V. Logie, M. Peter, P. Wehrer, L. Hilaire, and G. Maire, J. Chim. Phys. Phys.-Chim. Biol. **94**, 1923 (1997).

[37] H. Jalili, N. F. Heinig, and K. T. Leung, J. Appl. Phys. **105**, 034305 (2009).